Journal of Materials Chemistry C

ROYAL SOCIETY OF CHEMISTRY

PAPER

View Article Online
View Journal | View Issue

Cite this: J. Mater. Chem. C, 2023, 11, 6026

Structural control of charge transport in polymer monolayer transistors by a thermodynamically assisted dip-coating strategy†

Chenming Ding,[ab] Junyang Deng,[a] Miao Cheng,[a] Mengmeng Li *[ab] and Ling Li[a]

Received 15th February 2023,
Accepted 12th April 2023

DOI: 10.1039/d3tc00562c

rsc.li/materials-c

Since most charge transport in organic field-effect transistors occurs within the first molecular layer close to the dielectric layer, monolayer transistors become an ideal platform for transport investigation. Considerable efforts have been made to obtain high-performance monolayer transistors for conjugated small molecules, but the realization of high-mobility (over 0.5 $cm^2 V^{-1} s^{-1}$) polymer monolayers still remains challenging due to low crystallinity and difficulties in morphology control of conjugated polymers. In this work, the thermodynamic process of natural cooling of polymer solutions from elevated temperatures (T_e) is investigated, which is found to play a critical role in the polymer aggregation behavior and film morphology during dip-coating from such warm solutions. The polymer aggregation of the solutions decreases with increasing T_e from room temperature to 50 °C, but the maximum aggregate growth rate is observed at T_e = 40 °C. The monolayer formed at T_e = 40 °C exhibits a higher degree of molecular order with larger nanofibers, resulting in a twofold increase in the saturation mobility in resulting monolayer transistors. In addition, the effect of channel length on the T_e effect is also studied. These results open new pathways to further understand the structure–property relationship and to boost the device performance of organic electronics.

Introduction

With the rapid development of the Internet of Things (IoT) era, the demand for multi-module, intelligent and wearable portable electronic devices is growing dramatically. Compared with their inorganic counterparts, organic semiconductors have received widespread attention because of their unique advantages such as intrinsic flexibility, good biocompatibility, low cost and large-scale manufacturing at low temperatures. As a result, they hold great potential for applications in biomedical, flexible wearable, and display fields.[1–8]

In recent years, it has been widely reported that in organic field-effect transistors (FETs), most carrier transport occurs in the first molecular layer in contact with the gate dielectric.[9–11] Therefore, FETs with their active layer thickness downscaled to a single molecular layer (monolayer) have become a favourable tool to study the charge transport properties due to the two-dimensional (2D) pathway (Scheme 1). Generally, semiconducting small molecules possess higher crystallinity than conjugated polymers, and the corresponding monolayer FETs have been realized with high performance.[12–14] For instance, field-effect mobilities of the furan-thiophene quinoidal compound (TFT-CN)[15] and 1,4-bis((5′-hexyl-2,2′-bithiophen-5-yl)ethynyl)benzene (HTEB)[10] monolayer FETs have reached more than 1 $cm^2 V^{-1} s^{-1}$. Moreover, a mobility of over 10 $cm^2 V^{-1} s^{-1}$ was also reported for monolayer FETs based on 3,11-dioctyldinaphtho[2,3-*d*:2,3′-*d*′]benzo[1,2-*b*:4,5-*b*′]dithiophene (C8-DNBDT-NW)[16] and 2,7-dioctyl-[1]benzothieno[3,2-*b*][1]benzothiophene (C8-BTBT).[17] Furthermore, n-type small molecule monolayer FETs with electron mobilities of over 1 $cm^2 V^{-1} s^{-1}$ were also reported.[12,18] However, the fabrication of conjugated polymer monolayer FETs with high field-effect mobility (over 0.5 $cm^2 V^{-1} s^{-1}$) over large areas remains challenging due to lower crystallinity of conjugated polymers and the associated difficulties of efficient morphology control.[19]

The microstructure of most conjugated polymers exhibits a combination of both semi-ordered and amorphous 'spaghetti-like' regions. The semi-ordered region is mainly responsible for the charge transport, critically affecting the resulting FET performance.[19,20] The aggregation behaviour of conjugated polymers in solutions plays a significant role in film formation and subsequent film morphology.[20,21] Note that another advantage of organic semiconductor monolayers is that their surface topography can directly reflect their structural information compared to

[a] Key Laboratory of Microelectronic Devices and Integrated Technology, Institute of Microelectronics, Chinese Academy of Sciences, 100029 Beijing, China. E-mail: limengmeng@ime.ac.cn
[b] University of Chinese Academy of Sciences, 100049 Beijing, China

† Electronic supplementary information (ESI) available. See DOI: https://doi.org/10.1039/d3tc00562c

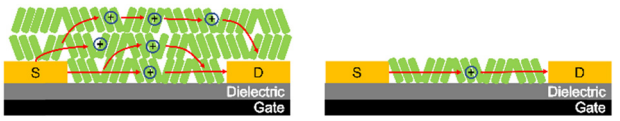

3D 2D

Scheme 1 Schematic illustration of charge transport in organic semiconducting multilayer (left) and monolayer (right) FETs with three-dimensional (3D) and 2D transport.

multilayers that can have vertical anisotropy in morphology.[22–24] For semiconducting polymers with a strong temperature-dependent aggregation behaviour,[25–28] it was revealed that besides extensively studied solution temperature, the temperature that was used to dissolve the polymer in solvents also had significant impacts on the conformation of polymer backbones. With decreasing dissolution temperature, the fibril width of the resulting polymer monolayer was almost doubled, resulting in the remarkable enhancement in FET performance.[21] In addition, the solution processing during which the solution remains at high temperatures for aggregation control was also proposed for the fabrication of organic semiconducting ultrathin layers, but the resulting non-uniform thickness of the obtained films caused severe hindrance in understanding the intrinsic structure–property relationship.[29]

In this study, the microstructure of a single molecular layer of a conjugated polymer, poly[(5,6-difluoro-2,1,3-benzothiadiazole-4,7-diyl)[3,3‴-bis(2-decyltetradecyl)[2,2′:5′,2″:5″,2‴-quaterthiophene]-5,5‴-diyl]] (PffBT4T-2DT), was precisely controlled through a thermodynamically assisted strategy, where the dip-coating process was conducted in a warm solution that was cooled down naturally from elevated temperatures (T_e). Compared to room temperature (RT), the elevated temperature is unconducive to polymer aggregation in solution to a certain extent, but allows the fine tuning of the growth rate of aggregates. The kinetic characterization studies for the naturally cooled solutions revealed that at the initial stage, the growth rate of aggregates changes rapidly, but starting from around 55 s more than 90% of the aggregates form and the growth rate remains almost constant, which is also the moment when the film formation takes place. It is found that the highest growth rate can be achieved at T_e = 40 °C, well consistent with the theoretical analysis. Furthermore, at T_e = 40 °C PffBT4T-2DT thin films exhibit larger coherence length and smaller paracrystallinity than at other T_e values and even at RT, indicative of a higher degree of molecular order. More importantly, the fibril dimensions of the dip-coated polymer monolayer show an identical trend. Larger fibrils with a width of 38 nm are obtained at T_e = 40 °C, which is double that obtained at RT. Consequently, an increase in the saturated mobility of the resulting FET by a factor of 2 is observed. Additionally, the impact of channel length of FETs was also investigated. The thermodynamically assisted method proposed in this work is not only capable of efficiently controlling the growth rate of polymer aggregates and subsequently film morphology, but also provides further understanding of charge transport in organic electronics.

Experimental

Materials

PffBT4T-2DT (M_n = 116.4 kg mol^{-1} and M_w/M_n = 1.87) was purchased from Nanjing Zhiyan Ltd and used without further purification. Gel permeation chromatography (GPC) at 150 °C was performed with 1,2,4-trichlorobenzene as the eluent. Polymer solutions were heated to certain temperatures (30, 40 and 50 °C) on a hotplate for 10 min, and then cooled down naturally on a laboratory table (t = 0). At t = 55 s, the substrate was pulled out from this solution for the fabrication of polymer monolayers.

Optical spectroscopy

Steady-state UV-vis-NIR absorption spectra were recorded for polymer solutions at various temperatures and monolayer thin films formed at various T_es using a PerkinElmer Lambda 1050 instrument. The time-resolved measurement for the relevant kinetic process of 0–0 peak absorbance was performed using a Horiba Duetta instrument. Polymer solutions were heated to certain temperatures (30, 40 and 50 °C) on a hotplate for 10 min, and then transferred to the sample holder of the Horiba Duetta instrument. Immediately, the measurements were conducted with a sampling interval of 1 s.

Surface characterization

Atomic force microscopy (AFM) images of PffBT4T-2DT monolayers were recorded in air by using a Bruker MultiMode-V instrument in a peak force tapping mode. AFM images were processed by using AFM analysis software Gwyddion.

OFET fabrication and testing

Bottom-gate, bottom-contact FETs with channel length (L)/width (W) = 20 were fabricated on heavily doped silicon substrates coated with 300 nm-thick thermally grown silicon dioxide. These silicon substrates were used as gate electrodes and thermally grown silicon dioxide as the dielectric layer. Then 35 nm-thick Ti/Au (5/30 nm) electrodes were patterned on the substrates as source and drain electrodes using the conventional photolithography technique. PffBT4T-2DT monolayers were deposited by dip-coating from a 0.5 mg mL^{-1} solution in chloroform. After deposition, PffBT4T-2DT monolayers were annealed at 100 °C for 30 min in a glovebox under a nitrogen atmosphere to ensure the removal of the residual solvent. Note that such treatment has a negligible effect on the molecular order.[25] A Keithley 4200-SCS system was used for all electrical measurements in a glovebox.

Results and discussion

For conjugated polymorphs, the molecular solvation state is characterized from a single broad absorption peak in the UV-vis-NIR absorption spectrum, while in the aggregated state, a red shift is generally observed due to the planarization of the polymer backbone, accompanied by the appearance of a vibrational peak or shoulder.[30–32] PffBT4T-2DT was selected as the model compound in this work due to its strong temperature-dependent aggregation behavior (inset in Fig. 1a).[25,27,33]

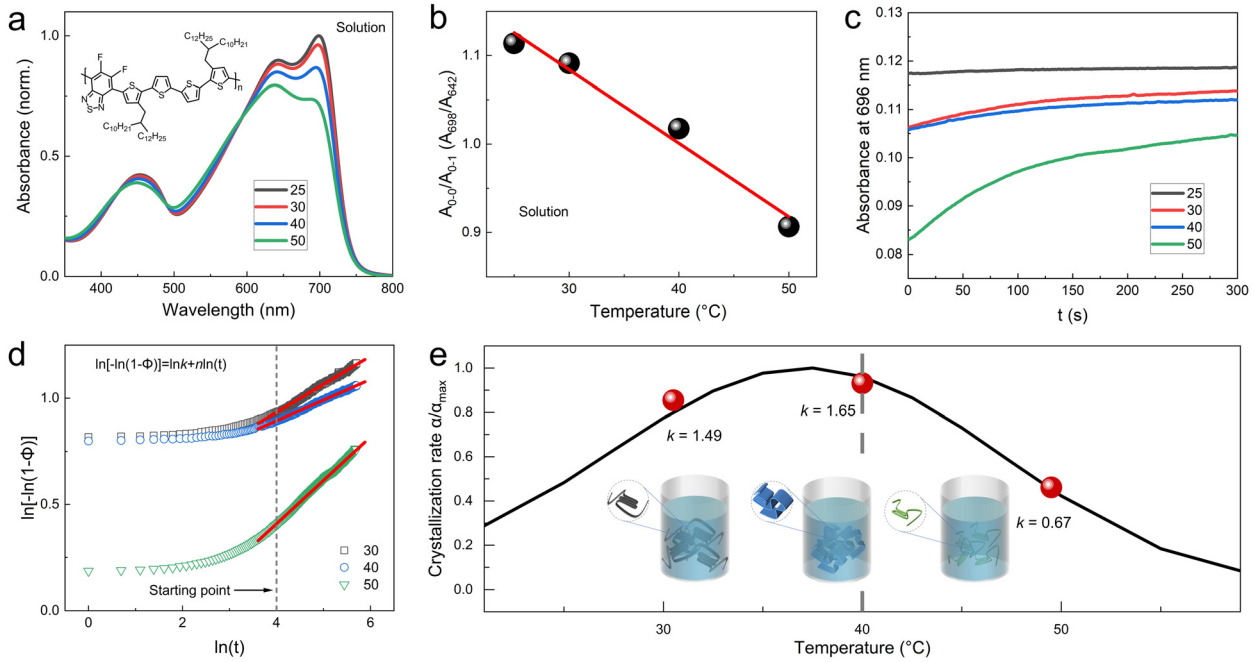

Fig. 1 (a) UV-vis-NIR absorption spectra of PffBT4T-2DT solutions in chloroform at various temperatures (25, 30, 40 and 50 °C). The polymer concentration in solution is 0.5 μM. The inset shows the chemical structure of PffBT4T-2DT. (b) Corresponding absorbance ratio of the 0–0 (698 nm) to the 0–1 peak (642 nm) as a function of temperature. (c) Evolution of 0–0 peak absorbance of naturally cooled warm solutions at various T_es. Experimental errors exist for t = 0 s due to (1) the rapid heat transfer from quartz cuvettes (warm solution) to metal holders in the UV-vis-NIR instrument and (2) a time difference of around 5 s is taken by removing the cuvette from the hotplate to sample holders and measurement startup. (d) Relationship between the fraction of the transformed aggregation (Φ) and evolution time (t) at various T_e values. (e) Relationship between the relative crystallization rate (black line) and T_e. The red solid balls indicate the growth rate of aggregates extracted from the Avrami equation.

Fig. 1a shows the UV-vis-NIR absorption spectra of PffBT4T-2DT in a chloroform solution at different temperatures, and it is clear that the elevated temperature severely affects the aggregation behavior of PffBT4T-2DT in solution. At RT (25 °C), the absorption spectrum was similar as that in the solid state (will be discussed), where the intensity of the 0–0 peak at 698 nm was greater than that of the 0–1 peak at 642 nm, indicating the J-aggregation phenomenon.[34] In contrast, the increase in solution temperature led to a noticeable reduction in the intensity ratio of the 0–0 to 0–1 peak (A_{0-0}/A_{0-1}). This could be well described using the order–disorder transition model, where the planarization of polymer backbones was degraded with increasing solution temperature.[32] It is worth noting that at an elevated solution temperature above 40 °C, the A_{0-0}/A_{0-1} ratio decreased to below 1 (Fig. 1b). On the other hand, these warm solutions at elevated temperatures were cooled down naturally, and the relevant kinetic process was studied by real-time monitoring of 0–0 peak absorbance (Fig. 1c). Apparently, distinct behaviors of polymer aggregation were observed, which was further analyzed using the Avrami theory. It must be emphasized that this Avrami equation[35] has been successfully utilized to describe the nucleation and growth processes of conjugated polymers in solution,[21,36] which is given as follows

$$\Phi = 1 - e^{(-kt^n)} \quad (1)$$

where Φ is the fraction of transformed aggregation at time t, n is the Avrami index, and k is the growth rate of the aggregation. This equation is usually expressed in logarithmic form to conveniently extract k values from the data.

$$\ln[-\ln(1 - \Phi)] = \ln k + n \ln(t) \quad (2)$$

Herein, the value of Φ can be estimated from A/A_{max}, where A is the absorbance of the 0–0 peak at time t, and A_{max} the absorbance of the 0–0 peak when the aggregation growth is complete (*i.e.*, RT solution). It is evident from Fig. 1d that this Avrami equation accurately describes the growth and aggregation of the polymer at different T_e values. In general, two regions can be divided with the turning point at $\ln t = 4$ (~55 s, which is also selected as the starting point for dip-coating and will be discussed). At the initial stage (low $\ln t$), the growth rate k (intercept of the red line in Fig. 1d) changes rapidly. In comparison, at $\ln t$ above 4, the k value remains almost constant. Interestingly, it was found that the growth rate of PffBT4T-2DT aggregation after $\ln t = 4$ is dependent on T_e, with the maximum k of 1.65 at T_e = 40 °C (Table 1).

In addition to the Avrami model, the aggregation of PffBT4T-2DT in solution can also be fitted using the Schmelzer equation:[37]

$$\left.\frac{d}{dT}(Ju^n)\right|_{T=T_{max}^{(overall)}} = 0 \quad (3)$$

where the T is the temperature, J is the function of the nucleation rate at various T values (eqn (S1), ESI†), u is the function of the growth rate at various T values (eqn (S2), ESI†), and n is the number of independent directions of growth. Because u, J, and n

Table 1 Characterization summary of the PffBT4T-2DT solution, monolayer and resulting FET at various T_e values

T_e[a] [°C]	25	30	40	50
k[b]	—	1.49	1.65	0.67
L_{CL}[c] [nm]	13.20	—	15.94	14.60
g[d] [%]	15.71	—	14.57	15.14
Fibril width [nm]	17.79	31.28	38.19	27.95
Mobility[e] [$cm^2 V^{-1} s^{-1}$]	0.29	0.60	0.67	0.50
Reliability factor[e]	0.84	0.87	0.80	0.89
Threshold voltage[e] [V]	−6.77	−6.14	−2.97	0.03
SS[ef] [V dec^{-1}]	1.02	2.61	0.65	1.16
On/off ratio[e]	10^7	10^5	10^8	10^7

[a] Elevated temperature. [b] Growth rate of the aggregation. [c] Coherence length. [d] Paracrystallinity parameter. [e] Extracted from the transfer curves of the L = 10 μm FETs. [f] Subthreshold swing.

are positive, from eqn (3) and eqn (S1), (S2) (ESI†), it can be seen that for polymer solutions there exists a maximum overall crystallization rate temperature. Fig. 1e exhibits that the growth rate of PffBT4T-2DT (k values extracted from the Avrami model) in solution is well consistent with this model (solid line). The crystallization rate rises and then falls, and the maximum is observed at around T_e = 40 °C.

The dip-coating technique that allows for precise control of the film microstructure with monolayer precision[23,24,38,39] was employed to fabricate PffBT4T-2DT monolayers. Different from previous publications,[21,29,39] warm solutions were obtained at various T_e values and then naturally cooled down (defined the starting of cooling as t = 0 s), and the dip-coating was performed at t = 55 s due to the following considerations (Fig. 2a). On one hand, at t = 55 s more than 90% aggregates were formed (Fig. 1c) but there was still sufficient room for reorganization of polymer self-assembly. On the other hand, compared to t = 0 s, only small temperature differences (<8%) were observed at t = 55 s for all T_e values (Fig. 2d). Note that this thermodynamically assisted method is different from dip-coating directly from hot solution, which resulted in non-uniform thin films.[29] The optimized dip-coating speed for PffBT4T-2DT monolayers was 50 μm s^{-1}. It is evident from Fig. 2b that the monolayer films show identical

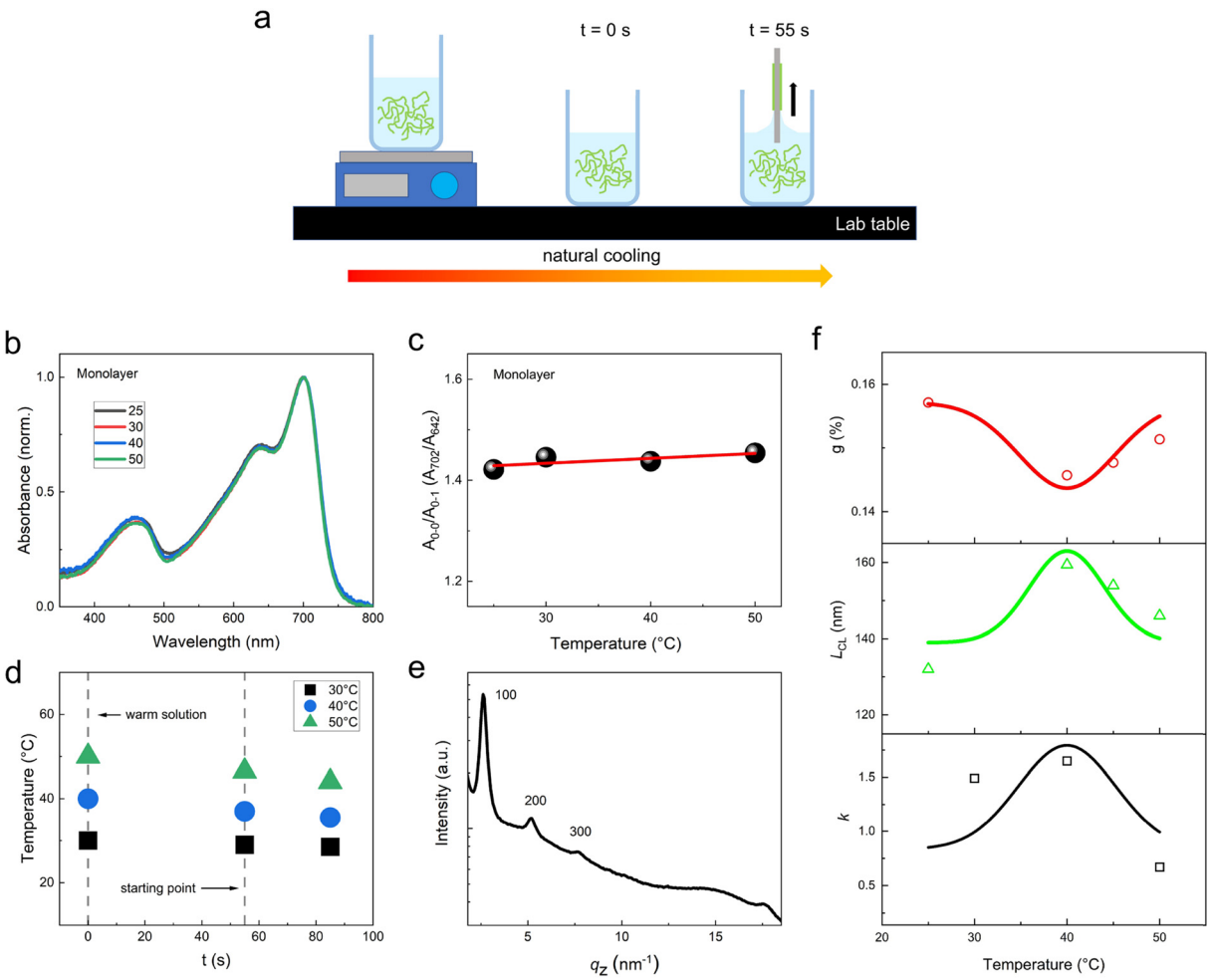

Fig. 2 (a) Schematic illustration of polymer monolayer fabrication by a thermodynamically assisted dip-coating strategy. The heated polymer solution was cooled down naturally on a laboratory table. At t = 55 s, the substrate was pulled out from this solution. (b) UV-vis-NIR absorption spectra of polymer monolayers formed at various T_e values (25, 30, 40, and 50 °C). The monolayers were dip-coated from a 0.5 mg mL^{-1} chloroform solution at a speed of 50 μm s^{-1}. (c) Corresponding absorbance ratio of the 0–0 to the 0–1 peak as a function of T_e of polymer monolayers. (d) Evolution of solution temperature during natural cooling. (e) 1D GIWAXS out-of-plane profile of thin films of PffBT4T-2DT at T_e = 40 °C. (f) k, L_{CL} and g as a function of T_e.

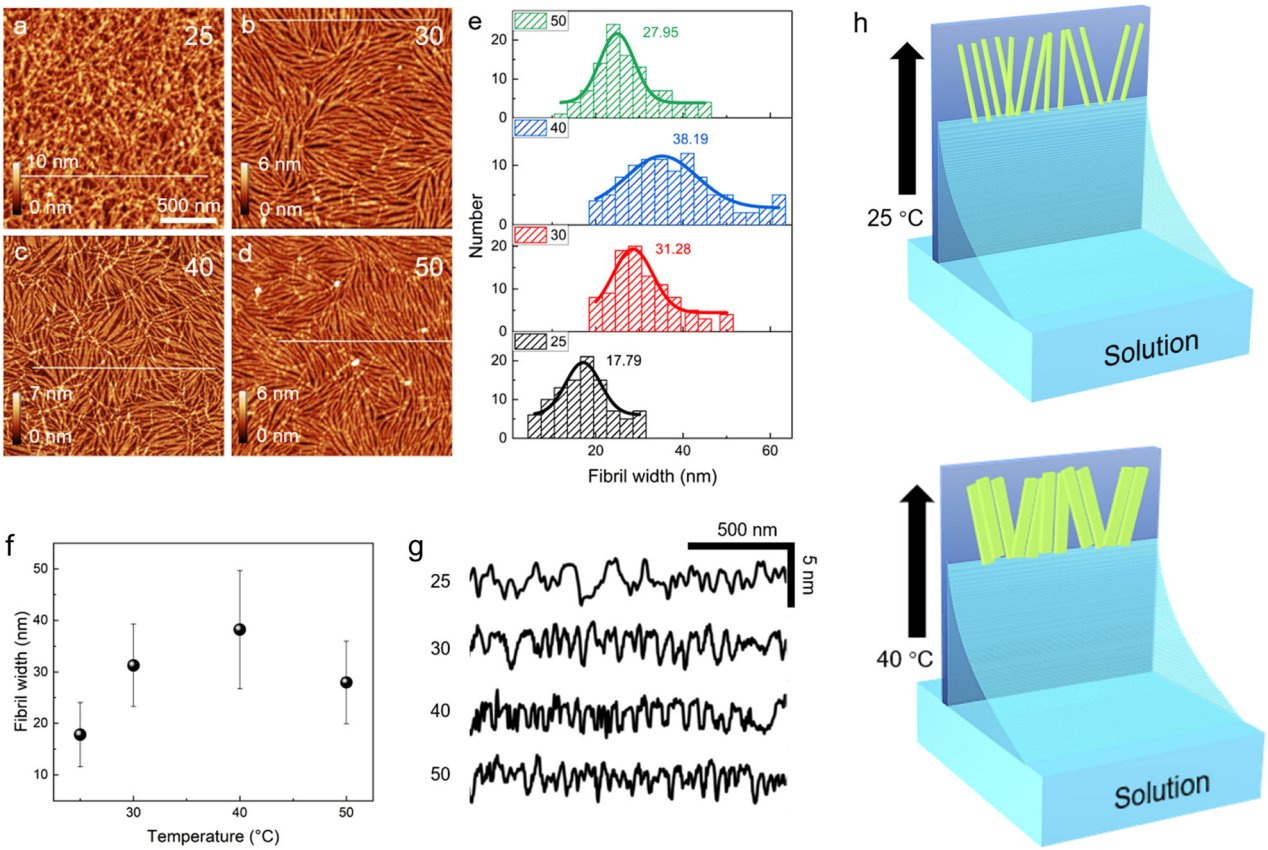

Fig. 3 (a–d) AFM height images of PffBT4T-2DT monolayers dip-coated at different T_e values. All AFM images share the same scale bars. (e) Distributions of the fibril width extracted from the AFM height images. (f) Fibril width as a function of T_e. The average values and standard deviation for each sample are analyzed from over 100 fibrils. (g) Corresponding height profiles of the white lines in (a)–(d). (h) Schematic diagram of fibril growth (polymer monolayer) at different T_e values (25 °C and 40 °C).

absorption spectra with strong J-aggregation, independent of T_e, and A_{0-0}/A_{0-1} reaches 1.4 (Fig. 2c). Compared to polymer solutions, such a value is increased by around 20%, and a redshift of the 0–0 peak by 3 nm is visible, indicating higher molecular order and larger conjugation length. This can be attributed to the enhanced π–π stacking interaction between polymer backbones.

Due to the challenges of X-ray measurement for monolayers, the effect of solution/processing temperatures on structural information was explored by performing grazing incidence wide-angle X-ray scattering (GIWAXS) for PffBT4T-2DT thin films. All samples exhibited similar edge-on texture with pronounced high-order (h00) reflections (Fig. 2e and Fig. S1, ESI†). Detailed analysis was carried out for (100) reflection, and the corresponding coherence length (L_{CL}) and the paracrystallinity parameter (g) were evaluated using the following equations:

$$L_{CL} = \frac{2\pi K}{\Delta q} \quad (4)$$

$$g = \sqrt{\frac{\Delta q}{2\pi q_0}} \quad (5)$$

where Δq is the full width at half maximum of the peak, K is a shape factor with the empirical value of 0.9 and q_0 is the center position of the peak. It is clear that the film processed at T_e = 40 °C exhibits the largest coherence length and lowest paracrystallinity (Fig. 2f and Table 1). These results demonstrate that T_e = 40 °C is conducive to generating a higher degree of molecular order, in well accordance with the aggregate growth rate in solution (Fig. 1e).

To elucidate the impact of T_e on the morphology of polymer monolayers in more detail, atomic force microscopy (AFM) was employed, and the corresponding surface topographies are shown in Fig. 3a–d. The thickness of dip-coated ultrathin films was around 3 nm (Fig. 3g), which is equivalent to the interlayer spacing of edge-on oriented multilayers and can therefore be defined as a monomolecular layer.[24] For the monolayer prepared at T_e = 25 °C (Fig. 3a), the resulting fibril width was statistically about 17.79 ± 6.23 nm. The presence of a small portion of bright domains in the AFM image indicates the beginning of the second monolayer growth. As T_e increases, a similar fibril microstructure is obtained but the fibril width is gradually enhanced (Fig. 3b and c). At T_e = 40 °C, the fibril width reaches a peak with a value of 38.19 ± 11.49 nm (Fig. 3e). Afterwards, a higher T_e (50 °C) leads to a slight reduction in fibril width to 27.95 ± 8.06 nm. This trend of fibril width is in good agreement with k values extracted from the in-time absorption spectra (Fig. 1e and Table 1). Therefore, it can be

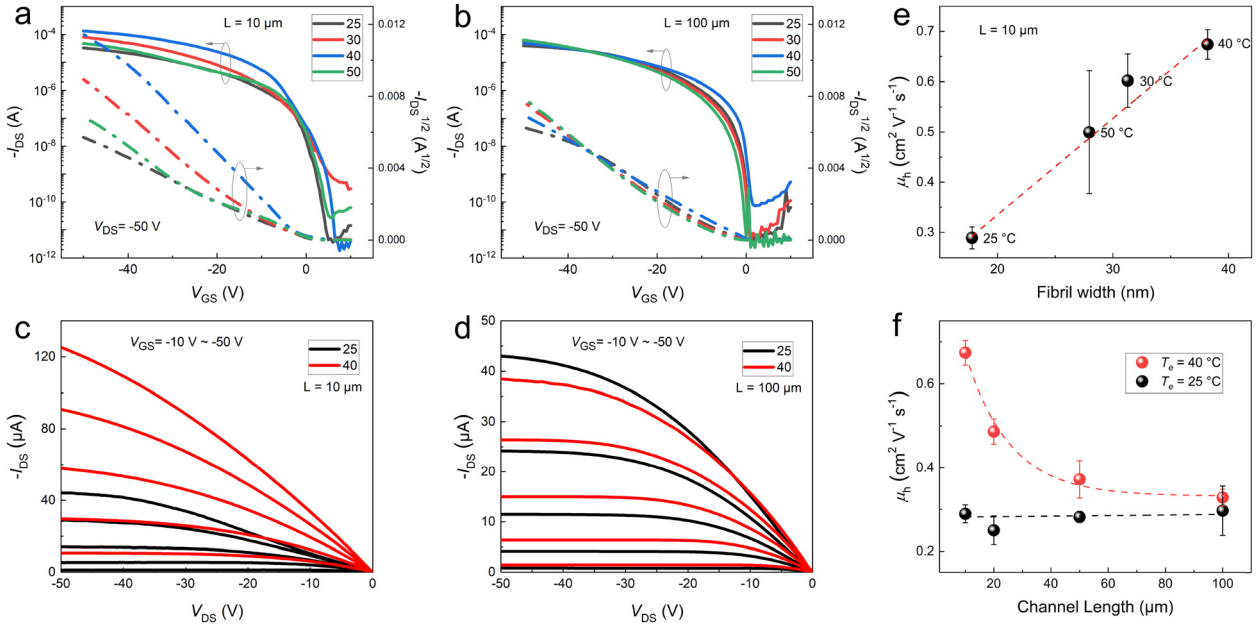

Fig. 4 (a) Transfer characteristics of PffBT4T-2DT monolayer FETs (L = 10 μm) dip-coated at various T_e values (25, 30, 40, and 50 °C). The drain voltage (V_{DS}) is −50 V. On-current (I_{on}) is defined as the drain–source current (I_{DS}) at gate–source voltage (V_{GS}) = −50 V. (b) Transfer characteristics of PffBT4T-2DT monolayer FETs (L = 100 μm) at various T_e values (25, 30, 40, and 50 °C). (c) Output characteristics of the PffBT4T-2DT monolayer FET (L = 10 μm) at T_e = 25 °C (black) and 40 °C (red). (d) Output characteristics of the PffBT4T-2DT monolayer FET (L = 100 μm) at T_e = 25 °C (black) and 40 °C (red). (e) Saturated field-effect mobility (μ_h) of L = 10 μm FETs as a function of fibril width. (f) μ_h as a function of channel length (10, 20, 50 and 100 μm). T_e = 25 °C and 40 °C.

concluded that the larger nanofibrils at T_e = 40 °C originate from the higher aggregate growth rate in solution (Fig. 3h).

The relationship between the microstructure and charge transport for these polymer monolayers is explored by fabricating bottom-gate bottom-contact FETs with 300 nm-thick SiO_2 as the dielectric layer. Prior to polymer monolayer deposition, Au electrodes are patterned onto the Si/SiO_2 substrate, acting as source and drain electrodes. It has to be emphasized that the surface modification using self-assembled monolayers (SAMs) is neither applied for Au electrodes nor SiO_2 dielectrics, since the elevated temperatures could cause different interactions between SAMs and polymers.

The transfer and output characteristics of the resulting polymer monolayer FETs exhibited a typical linear/saturation behavior (Fig. 4). In particular, the improvement of the FET performance was observed by applying different T_es. As shown in Fig. 4a, in the FETs with a 10 μm channel length, the drain-current (I_{DS}) is strongly dependent on T_e. Apparently, the I_{DS} of the FET obtained at T_e = 40 °C is higher than that obtained at T_e = 25 °C. When the gate voltage (V_{GS}) is increased to −50 V, the on-current (I_{on}) difference between them roughly reaches a factor of 4. Such a trend is also visible in output curves, in which I_{DS} of the FET formed at T_e = 40 °C is 125 μA, much higher than 44 μA for the FET formed at T_e = 25 °C (Fig. 4c). As a result, the corresponding saturated hole-mobilities (μ_h) extracted from the transfer curves for T_e = 40 °C (0.67 ± 0.03 $cm^2 V^{-1} s^{-1}$) is twofold higher than that at T_e = 25 °C (0.29 ± 0.02 $cm^2 V^{-1} s^{-1}$, Fig. 4e). It seems that T_e = 40 °C is a threshold value after which the mobility drops by 25% to 0.50 ± 0.12 $cm^2 V^{-1} s^{-1}$ for T_e = 50 °C. It is worth noting that this mobility dependence on T_e is similar with the trend of fibril width. The accuracy of extracted mobility can be evaluated using reliability factor γ,[40] which is defined as the ratio of the extracted mobility from the transfer curve to that of an electrically equivalent FET that follows the ideal Shockley behavior. As shown in Fig. S2 (ESI†) and Table 1, an average value of around 0.85 indicates the high confidence of our extracted mobility. Additionally, the monolayer FET from T_e = 40 °C also exhibits a relatively good threshold voltage and a better subthreshold swing and on/off current ratio (Table 1).

To further investigate the effect of T_e on device performance, the contact resistance of the monolayer FETs with different T_e values was evaluated using the transmission line method (TLM) (Fig. S3, ESI†). The results show that the contact resistance remains almost constant (~kΩ cm), independent of T_e. Such a high value can be attributed to the absence of SAM modification for FET devices. The morphology of the monolayer on the source–drain electrodes was also characterized by AFM, and negligible effects from T_e could be observed (Fig. S4, ESI†). All these results demonstrate that the enhanced FET performance originates from the improvement of fibril width within the monolayer induced by T_e. The effect of T_e on charge transport in FETs with different channel lengths (20 μm, 50 μm and 100 μm) was also investigated (Fig. 4b and Fig. S5, ESI†). The dependence of saturated mobility on T_e and channel length (L) are plotted in Fig. 4f and Fig. S6 (ESI†). It was found that the effect of T_e on the charge transport becomes negligible in FETs with longer channels. As shown in Fig. 4b and d, in the 100 μm

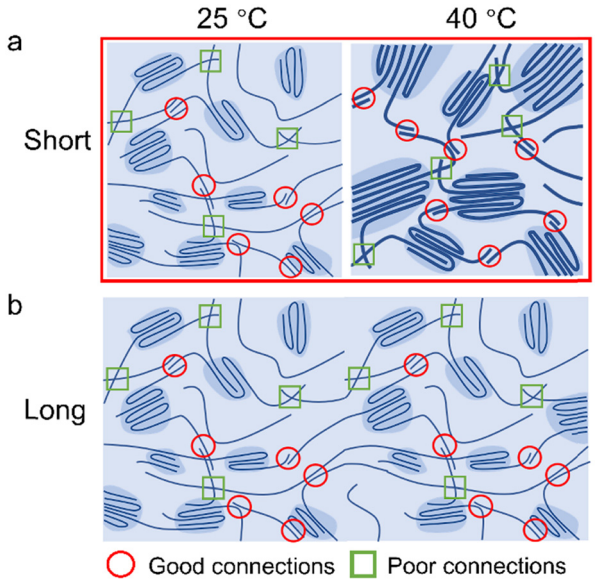

Fig. 5 Schematic illustration for the microstructure of conjugated polymer films, where crystalline domains exist with good/poor connections between them.

FETs, the drain-current of the FETs are unaffected by T_e at $V_{GS} = -50$ V.

It is widely reported that a larger domain size is beneficial to the charge transport in polymer FETs (Fig. 5a).[23,39,41] This conclusion is further supported by our FET results, where the saturated mobility of polymer monolayer FETs with short channels (10 μm) is almost proportional to the fibril width (Fig. 4e). In contrast, the connections between highly ordered crystalline domains, that mainly include the good connections (red circles in Fig. 5) formed by π–π stacking between polymer backbones and the poor connections (green squares in Fig. 5), play more important roles in charge transport for long-channel FETs.[42,43] In long channel devices (Fig. 5b), the presence of more poor connections is evident, and the contribution of larger domain size (fibril width) induced by T_e to charge transport is negligible compared to the current of the conducting channel. This perfectly explains the similar mobility values for the monolayer FETs with $L = 100$ μm, independent of T_e (Fig. 4f).

The influences of dip-coating speed and polymer concentration were also investigated.[44–46] It is obvious from Fig. S7 (ESI†) that faster dip-coating speeds (200 μm s^{-1} and 800 μm s^{-1}) generally lead to the formation of ultrathin films with a lower degree of molecular order, so that the corresponding mobility is significantly reduced (Fig. S8, ESI†). On the other hand, lower polymer concentration (0.1 mg mL^{-1}) can hardly result in generation of a fibril nanostructure, resulting in the degradation of FET performance by orders of magnitude. Additionally, under the conditions of fast dip-coating speed and low polymer concentration, the effect of T_e is not visible.

Conclusions

In conclusion, a novel and effective processing method, thermodynamically assisted dip-coating, is proposed to realize the high-mobility polymer monolayer FETs. It is found that the kinetic process of natural cooling of the polymer solution allows the fine control of the aggregate growth rate. At $t = 55$ s, 90% aggregation is complete, and afterwards an almost constant growth rate is observed. The highest growth rate can be achieved at $T_e = 40$ °C, in excellent agreement with coherence length and paracrystallinity of corresponding thin films. More importantly, the fibril width of dip-coated monolayers is twofold higher than that at RT, resulting in significant improvement in FET performance. These findings offer further understanding of the structure–property relationship, and provide a new strategy to boost the performance of organic electronic devices.

Author contributions

M. L. conceived the idea for this study; C. D. and J. D. performed UV-vis-NIR and AFM measurements; C. D. conducted the theoretical fitting; C. D. fabricated transistors and carried out electrical measurements. M. L. supervised the project. All authors commented on the data and co-wrote the manuscript.

Conflicts of interest

There are no conflicts to declare.

Acknowledgements

This work was supported by the National Key R&D Program of China (grant no. 2019YFA0706100, 2020YFA0210800, and 2021YFA0909400), the National Natural Science Foundation of China (grant no. 62074163, 61890944, 61888102, 61720106013, and 22025402) and the Strategic Priority Research Program of Chinese Academy of Sciences (grant no. XDB30030000, XDB30030300, and XDB44000000). This work was carried out with the support of the 1W1A beamline at the Beijing Synchrotron Radiation Facility.

References

1 G. Schwartz, B. C.-K. Tee, J. Mei, A. L. Appleton, D. H. Kim, H. Wang and Z. Bao, *Nat. Commun.*, 2013, **4**, 1859.
2 C. Wang, D. Hwang, Z. Yu, K. Takei, J. Park, T. Chen, B. Ma and A. Javey, *Nat. Mater.*, 2013, **12**, 899–904.
3 K. Myny, *Nat. Electron.*, 2018, **1**, 30–39.
4 S. Wang, J. Xu, W. Wang, G.-J. N. Wang, R. Rastak, F. Molina-Lopez, J. W. Chung, S. Niu, V. R. Feig and J. Lopez, *Nature*, 2018, **555**, 83–88.
5 M. Sugiyama, T. Uemura, M. Kondo, M. Akiyama, N. Namba, S. Yoshimoto, Y. Noda, T. Araki and T. Sekitani, *Nat. Electron.*, 2019, **2**, 351–360.
6 E. Li, C. Gao, R. Yu, X. Wang, L. He, Y. Hu, H. Chen, H. Chen and T. Guo, *Nat. Commun.*, 2022, **13**, 2898.
7 N. Luo, P. Ren, Y. Feng, X. Shao, H.-L. Zhang and Z. Liu, *J. Phys. Chem. Lett.*, 2022, **13**, 1131–1146.

8 Y. Zhang, Y. Wang, C. Gao, Z. Ni, X. Zhang, W. Hu and H. Dong, *Chem. Soc. Rev.*, 2023, **52**, 1331–1381.
9 F. Dinelli, M. Murgia, P. Levy, M. Cavallini, F. Biscarini and D. M. de Leeuw, *Phys. Rev. Lett.*, 2004, **92**, 116802.
10 L. Jiang, H. Dong, Q. Meng, H. Li, M. He, Z. Wei, Y. He and W. Hu, *Adv. Mater.*, 2011, **23**, 2059–2063.
11 H. Li, Y. Li, H. Li and J. L. Brédas, *Adv. Funct. Mater.*, 2017, **27**, 1605715.
12 M. Xiao, J. Liu, C. Liu, G. Han, Y. Shi, C. Li, X. Zhang, Y. Hu, Z. Liu and X. Gao, *Nat. Commun.*, 2021, **12**, 2774.
13 J. Liu, Y. Yu, J. Liu, T. Li, C. Li, J. Zhang, W. Hu, Y. Liu and L. Jiang, *Adv. Mater.*, 2022, **34**, 2107574.
14 B. Peng, Z. He, M. Chen and P. K. L. Chan, *Adv. Funct. Mater.*, 2022, **32**, 2202632.
15 C. Wang, X. Ren, C. Xu, B. Fu, R. Wang, X. Zhang, R. Li, H. Li, H. Dong and Y. Zhen, *Adv. Mater.*, 2018, **30**, 1706260.
16 A. Yamamura, S. Watanabe, M. Uno, M. Mitani, C. Mitsui, J. Tsurumi, N. Isahaya, Y. Kanaoka, T. Okamoto and J. Takeya, *Sci. Adv.*, 2018, **4**, eaao5758.
17 C. Xu, P. He, J. Liu, A. Cui, H. Dong, Y. Zhen, W. Chen and W. Hu, *Angew. Chem., Int. Ed.*, 2016, **55**, 9519–9523.
18 Y. Shi, L. Jiang, J. Liu, Z. Tu, Y. Hu, Q. Wu, Y. Yi, E. Gann, C. R. McNeill and H. Li, *Nat. Commun.*, 2018, **9**, 2933.
19 M. Li, J. Wang, W. Xu, L. Li, W. Pisula, R. A. Janssen and M. Liu, *Prog. Polym. Sci.*, 2021, **117**, 101394.
20 R. Noriega, J. Rivnay, K. Vandewal, F. P. V. Koch, N. Stingelin, P. Smith, M. F. Toney and A. Salleo, *Nat. Mater.*, 2013, **12**, 1038–1044.
21 M. Li, H. Bin, X. Jiao, M. M. Wienk, H. Yan and R. A. J. Janssen, *Angew. Chem., Int. Ed.*, 2020, **59**, 846–852.
22 M. Campoy-Quiles, T. Ferenczi, T. Agostinelli, P. Etchegoin, Y. Kim and T. Anthopoulos, *Nat. Mater.*, 2008, **7**, 158–164.
23 M. Li, C. An, T. Marszalek, M. Baumgarten, K. Müllen and W. Pisula, *Adv. Mater.*, 2016, **28**, 2245–2252.
24 M. Li, D. K. Mangalore, J. Zhao, J. H. Carpenter, H. Yan, H. Ade, H. Yan, K. Müllen, P. W. Blom and W. Pisula, *Nat. Commun.*, 2018, **9**, 451.
25 Z. Chen, P. Cai, J. Chen, X. Liu, L. Zhang, L. Lan, J. Peng, Y. Ma and Y. Cao, *Adv. Mater.*, 2014, **26**, 2586–2591.
26 G. H. Heintges, P. J. Leenaers and R. A. Janssen, *J. Mater. Chem. A*, 2017, **5**, 13748–13756.
27 H. Hu, P. C. Chow, G. Zhang, T. Ma, J. Liu, G. Yang and H. Yan, *Acc. Chem. Res.*, 2017, **50**, 2519–2528.
28 R. Steyrleuthner, M. Schubert, I. Howard, B. Klaumünzer, K. Schilling, Z. Chen, P. Saalfrank, F. Laquai, A. Facchetti and D. Neher, *J. Am. Chem. Soc.*, 2012, **134**, 18303–18317.
29 G. Ouyang, H. Wu, X. Qiao, J. Zhang and H. Li, *ACS Omega*, 2018, **3**, 9290–9295.
30 B. M. W. Langeveld-Voss, M. P. T. Christiaans, R. A. J. Janssen and E. W. Meijer, *Macromolecules*, 1998, **31**, 6702–6704.
31 A. Köhler, S. T. Hoffmann and H. Bässler, *J. Am. Chem. Soc.*, 2012, **134**, 11594–11601.
32 F. Panzer, H. Bässler and A. Köhler, *J. Phys. Chem. Lett.*, 2017, **8**, 114–125.
33 J. Deng, L. Zheng, C. Ding, Y. Guo, Y. Xie, J. Wang, Y. Ke, M. Li, L. Li and R. A. Janssen, *Adv. Funct. Mater.*, 2023, **33**, 2209195.
34 F. C. Spano, *Acc. Chem. Res.*, 2010, **43**, 429–439.
35 M. Avrami, *J. Chem. Phys.*, 1940, **8**, 212–224.
36 N. E. Persson, P.-H. Chu, M. McBride, M. Grover and E. Reichmanis, *Acc. Chem. Res.*, 2017, **50**, 932–942.
37 J. W. P. Schmelzer, A. S. Abyzov, V. M. Fokin, C. Schick and E. D. Zanotto, *J. Non-Cryst. Solids*, 2015, **429**, 24–32.
38 J. Jang, S. Nam, K. Im, J. Hur, S. N. Cha, J. Kim, H. B. Son, H. Suh, M. A. Loth, J. E. Anthony, J.-J. Park, C. E. Park, J. M. Kim and K. Kim, *Adv. Funct. Mater.*, 2012, **22**, 1005–1014.
39 M. Li, F. Hinkel, K. Müllen and W. Pisula, *Nanoscale*, 2016, **8**, 9211–9216.
40 H. H. Choi, K. Cho, C. D. Frisbie, H. Sirringhaus and V. Podzorov, *Nat. Mater.*, 2018, **17**, 2–7.
41 N. Kleinhenz, N. Persson, Z. Xue, P. H. Chu, G. Wang, Z. Yuan, M. A. McBride, D. Choi, M. A. Grover and E. Reichmanis, *Chem. Mater.*, 2016, **28**, 3905–3913.
42 S. Y. Son, Y. Kim, J. Lee, G.-Y. Lee, W.-T. Park, Y.-Y. Noh, C. E. Park and T. Park, *J. Am. Chem. Soc.*, 2016, **138**, 8096–8103.
43 P. M. Beaujuge and J. M. Fréchet, *J. Am. Chem. Soc.*, 2011, **133**, 20009–20029.
44 L. Li, P. Gao, W. Wang, K. Mullen, H. Fuchs and L. Chi, *Angew. Chem., Int. Ed.*, 2013, **52**, 12530–12535.
45 K. Wu, H. Li, L. Li, S. Zhang, X. Chen, Z. Xu, X. Zhang, W. Hu, L. Chi, X. Gao and Y. Meng, *Langmuir*, 2016, **32**, 6246–6254.
46 Z. F. Yao, Y. Q. Zheng, Q. Y. Li, T. Lei, S. Zhang, L. Zou, H. Y. Liu, J. H. Dou, Y. Lu, J. Y. Wang, X. Gu and J. Pei, *Adv. Mater.*, 2019, **31**, e1806747.